Chinese Journal of
POLYMER SCIENCE

RESEARCH ARTICLE

https://doi.org/10.1007/s10118-026-3587-8
Chinese J. Polym. Sci.

Hetero-structured Poly(vinylidene fluoride)/$CsCuCl_3$ Nanofiber Composite Film *via* Coaxial Electrospinning for Human-Machine Interaction

Yi-Kai Zhao[a], Yi Zou[a], Jie-Chun Zhou[a], Jin-Rong Huang[a*], Jian-Wen Chen[a*], Jin-Rui Huang[b], and Yu-Tian Zhu[a*]

[a] *Key Laboratory of Organosilicon Chemistry and Material Technology, Ministry of Education, Zhejiang Key Laboratory of Organosilicon Material Technology, College of Material Chemistry and Chemical Engineering, Hangzhou Normal University, Hangzhou 311121, China*
[b] *Key Laboratory of Biomass Energy and Material, Jiangsu Province, Institute of Chemical Industry of Forest Products, Chinese Academy of Forestry, Nanjing 210042, China*

Electronic Supplementary Information

Abstract Polymer-based piezoelectric films can be assembled into piezoelectric nanogenerators (PENGs), which can simultaneously serve as flexible pressure sensors and energy harvesting devices. However, the low piezoelectric output of PENGs is a major limitation for their practical applications. Herein, we propose a coaxial electrospinning strategy to generate a core-shell structured nanofiber film, which could significantly enhance the piezoelectric output compared to the traditional nanofiber film *via* conventional single-axial electrospinning. Notably, the as-prepared PENGs based on the core-shell structured $CsCuCl_3$/poly(vinylidene fluoride) (PVDF) nanofiber composite film (2 wt%) produced *via* coaxial spinneret exhibit a 60% increase in output voltage (increase from 48 V to 75 V) and a 50% increase in short-circuit current (increase from 0.2 μA to 0.3 μA) compared to those prepared using a single-needle spinneret. More interestingly, this enhancement in piezoelectric performance is a universal phenomenon because the coaxial electrospinning process can induce greater polymer chain alignment in the shell layer and lead to increased crystallinity and a higher proportion of the piezoelectric-active *β*-phase. Owing to their enhanced piezoelectric output and high sensitivity to subtle pressure variations, the resulting PENGs demonstrate promising potential for human-machine interaction applications. This study offers a novel and broadly applicable approach to boost the piezoelectric performance of polymer-based PENGs.

Keywords Piezoelectric nanogenerators; Pressure sensors; Coaxial electrospinning; Piezoelectric performance; Human-machine interaction

Citation: Zhao, Y. K.; Zou, Y.; Zhou, J. C.; Huang, J. R.; Chen, J. W.; Huang, J. R.; Zhu, Y. T. Hetero-structured poly(vinylidene fluoride)/$CsCuCl_3$ nanofiber composite film *via* coaxial electrospinning for human-machine interaction. *Chinese J. Polym. Sci.* https://doi.org/10.1007/s10118-026-3587-8

INTRODUCTION

Flexible pressure sensors, which are essential components of wearable electronics and electronic skin systems, have attracted significant research interest in recent years owing to their capability to perceive pressure in real time.[1–6] Depending on their sensing mechanisms, these devices can be broadly classified into four categories: piezoresistive,[7–10] capacitive,[11–13] piezoelectric,[14–18] and triboelectric sensors.[19–22] Among these, piezoelectric sensors, also known as piezoelectric nanogenerators (PENGs), have emerged as a particularly promising option for flexible electronic applications owing to their simple device architecture, high sensitivity, and intrinsic self-powered functionality.

The operation of piezoelectric sensors is based on the piezoelectric effect of the piezoelectric layer, which converts mechanical energy into electrical energy. This intrinsic property enables the PENGs to function simultaneously as energy harvesters and pressure sensors. The piezoelectric layer in these sensors is typically composed of piezoelectric polymers, whereas poly(vinylidene fluoride) (PVDF) and its copolymers are the most commonly used materials. PVDF, a semicrystalline polymer, exists in five distinct phases: *α*, *β*, *γ*, *δ*, and *ε*, among which the *β*-phase exhibits a zigzag all-*trans* conformation with the highest dipole moment, thereby imparting superior piezoelectric properties.[23–25] Three strategies have been developed to enhance the piezoelectric performance of PVDF-based PENGs. The most straightforward approach is to induce the transition of non-piezoelectric phases to the piezoelectric *β*-phase. It has been reported that mechanical stretching under an electric field,[26] melt crystallization under high pressure,[27] and the incorporation of nucleating agents[28] can effectively facilitate the *α*-to-*β* phase transition, thereby improving the piezoelectric performance of the resulting PENGs. For example, Chang *et al.*[29] fabricated a piezo-

* Corresponding authors, E-mail: jinronghuang@hznu.edu.cn (J.R.H.)
E-mail: jwchen@hznu.edu.cn (J.W.C.)
E-mail: ytzhu@hznu.edu.cn (Y.T.Z.)
Received December 29, 2025; Accepted January 23, 2026; Published online April 16, 2026

electric PVDF nanofiber film *via* electrospinning, which demonstrated a significantly enhanced piezoelectric effect compared to conventional PVDF thin films. This enhancement was attributed to the electric field during electrospinning, which induced a phase transition from the inactive α phase to the piezoelectric β phase. The second strategy involves the incorporation of piezoelectric ceramic fillers, such as barium titanate ($BaTiO_3$),[30] zinc oxide (ZnO),[31] and GaN,[32] which typically possess higher piezoelectric coefficients than PVDF. These ceramics can be embedded into a polymer matrix to form hybrid piezoelectric composites with improved output performances and processabilities. For instance, Jiang *et al*.[33] incorporated $BaTiO_3$ into PVDF using electrospinning, resulting in nanocomposite films with a β -phase content of 91% and a 66% increase in the piezoelectric output compared to pristine PVDF films. The third strategy focuses on the addition of conductive fillers, such as MXene,[34] graphene (Gr),[35] and carbon nanotubes (CNTs), which could further increase the piezoelectric output of the resulting PENGs. For example, Zhang *et al*.[36] integrated MXene into PVDF nanofibers to fabricate an MXene/PVDF nanofiber film as the piezoelectric layer of PENGs, yielding a remarkable about 3.97-fold increase in piezoelectric output relative to pure PVDF films. Although these strategies significantly improve the piezoelectric performance of PVDF-based PENGs, their output levels remain insufficient to effectively power wearable electronics and portable devices. Therefore, it is desirable to develop new strategies for further enhancing the piezoelectric properties of polymer-based PENGs.

In this study, non-toxic and environmentally benign cesium copper chloride ($CsCuCl_3$) particles were synthesized *via* a hydrothermal method and subsequently incorporated into a PVDF matrix to fabricate hybrid $CsCuCl_3$/PVDF nanofiber films *via* electrospinning. Unlike conventional electrospun nanofiber films, a coaxial spinneret was employed in this study to produce core-shell structured $CsCuCl_3$/PVDF nanofibers. Notably, PENGs assembled using the core-shell structured $CsCuCl_3$/PVDF nanofiber film exhibited a remarkable 60% enhancement in piezoelectric output compared to those fabricated with traditional $CsCuCl_3$/PVDF nanofiber films. More importantly, this strategy demonstrates a broad applicability and can be extended to other systems. For instance, the same coaxial electrospinning approach led to an about 50% increase in the output for pure PVDF nanofiber films and an about 27% enhancement for ZnO/PVDF nanofiber films. Owing to the superior piezoelectric performance of core-shell structured $CsCuCl_3$/PVDF-based PENGs, these devices can be used for speech recognition and intelligent keyboards for playing computer games.

MATERIALS AND METHODOLOGY

Materials

Copric chloride dihydrate ($CuCl_2{\cdot}2H_2O$, 99.9%) and CsCl (99.99%) were obtained from Macklin Co., Ltd., and ZnO particles (size: 20–50 nm) were purchased from 3A Chem Technology Co., Ltd. PVDF ($M_w \approx 6\times10^5$ g/mol) was obtained from 3F New Materials Co., Ltd. Hydrochloric acid, *N*,*N*-dimethylformamide (DMF, analytical grade), isopropanol (IPA, analytical grade), and acetone (analytical grade) were purchased from Sinopharm Chemical Reagent Co., Ltd., China.

Synthesis of $CsCuCl_3$ Nanoparticles

$CsCuCl_3$ perovskite nanoparticles were synthesized using a solvothermal method. Briefly, 1 mmol (0.134 g) of $CuCl_2{\cdot}2H_2O$ was dissolved in 5 mL of hydrochloric acid to obtain a homogeneous solution. Then, 1 mmol (0.168 g) of CsCl was added to the solution and stirred for 15 min to obtain the precursor solution. Then, 50 mL of isopropanol was added to the precursor solution, followed by centrifugation at 6000 r/min for 5 min. The supernatant was discarded and the sediment was collected and dried in a vacuum oven at 60 °C to obtain $CsCuCl_3$ perovskite nanoparticles.

Fabrication of PVDF-based Nanofiber Films

Filler-doped PVDF-based nanofiber films

First, PVDF powder, DMF, and acetone were weighed and added to a sample bottle. The PVDF concentration was 12%, and the mass ratio of DMF to acetone was 4:6. The solution was stirred and $CsCuCl_3$ nanoparticles were added for ultrasonic treatment for 30 min to ensure uniform dispersion. The concentrations of $CsCuCl_3$ were 0.5 wt%, 1 wt%, 2 wt%, 3 wt%, 4 wt%, 5 wt%, and 10 wt%, respectively, and the corresponding nanofiber films were named as PCs 0.5 wt%-23 to PCs 10 wt%-23 (where the suffix indicates weight percentage and 23 denotes the 23-gauge spinneret needle used). Subsequently, the appropriate spinning solution was carefully loaded into a plastic syringe fitted with a 23G stainless steel needle in preparation for electrospinning. The syringe was then securely mounted onto an infusion pump set to deliver the solution at a constant flow rate of 1 mL/h. This flow rate was meticulously calibrated to correspond to the viscosity of the solution, thereby ensuring continuous and uniform deposition of the fibers. The distance between the tip of the spinneret and collector was precisely maintained at 15 cm. A high voltage ranging from 15 kV to 20 kV was applied to the needle. It is imperative to note that if the voltage is set too low, the electrospinning jet may become unstable, resulting in discontinuous fiber formation. Conversely, an excessively high voltage can lead to undesirable formation of beads within the fibers, which disrupts their uniformity. An optimal distance of 15 cm between the spinneret and collector is crucial, as it allows for sufficient stretching and solidification of the fibers. A shorter distance may result in incomplete solidification, whereas a longer distance can lead to unstable fiber formation.

The collector, which was covered with aluminum foil, was rotated at a constant speed of 300 r/min. The electrospinning process was carried out under controlled environmental conditions, specifically at room temperature, with the relative humidity (RH) meticulously regulated to remain within a narrow range of 30%±5%. This precise control of both temperature and humidity is essential to mitigate their potential effects on the morphological characteristics of the fibers, ultimately yielding a uniform and high-quality nanofiber membrane.

Core-shell structured PVDF-based nanofiber films

The PCs 2 wt%-23 spinning solution was chosen for the subsequent in-depth investigation. A coaxial spinneret was employed to fabricate PCs-23/18 using the aforementioned spinning solution for both the shell and core layers. Through spinnability experiments, the spinning speeds for the shell and

https://doi.org/10.1007/s10118-026-3587-8

core layers were precisely determined to be 0.5 and 1 mL/h, respectively. All other spinning parameters remained consistent with those outlined in Section *Filler-doped PVDF-based nanofiber films*, ensuring the reproducibility and reliability of the electrospinning process.

Assembly of Piezoelectric Sensors

The flexible PVDF-based nanofiber films were cut into 3 cm × 3 cm square blocks. A layer of copper foil was loaded on both sides of the square film and two copper wires were attached to the electrodes. Finally, two layers of PET film with a thickness of 0.1 mm were double-sided glued onto the top and bottom surfaces of the electrodes as protective layers for testing.

Characterizations and Measurements

The morphologies of the nanofiber film and $CsCuCl_3$ were meticulously visualized using a field-emission scanning electron microscope (SEM, Zeiss Supra55), while the fiber diameter was precisely analyzed using ImageJ software. To observe the dispersion of $CsCuCl_3$ within the PVDF nanofibers, an energy dispersive X-ray spectrometer (EDS, Zeiss Supra55) was used to observe. The β-phase crystals of the nanofiber films were thoroughly examined through Fourier transform infrared (FTIR, Nicolet5700) spectroscopy, with a scanning range of 4000–600 cm^{-1} and a resolution of 4 cm^{-1}, conducted in attenuated total reflection mode. The crystalline phase of the nanofiber films and the phase formation of $CsCuCl_3$ were characterized by X-ray diffraction (XRD, Rigaku Corporation Dmax2550). The crystallinity (χ_c) of the nanofiber films was determined by differential scanning calorimetry (DSC, Q100, TA) under nitrogen atmosphere at a heating rate of 5 °C/min from room temperature to 220 °C. The mechanical properties of the nanofiber films were rigorously tested using a universal testing machine (SUNS UTM 2502). Furthermore, the static water contact angles of the various film samples were accurately measured using a contact angle analyzer (DSA100, KRUSS). To capture the piezoelectric signals of the PENGs, a digital multimeter (DMM 7510, Keithley, USA) and digital electrometer (6514, Keithley, USA) were used under the periodic compression exerted by a linear motor (B01-37×120-C/C1100, NTI AG, USA).

RESULTS AND DISCUSSION

Microstructure and Characterization of PVDF/$CsCuCl_3$ Core-Shell Piezoelectric Nanofiber Films

The coaxial spinneret, comprising an inner needle for dispensing the core solution and an outer needle for dispensing the shell solution, enables the fabrication of core-shell structured nanofibers, as schematically illustrated in Fig. 1(a). In this study, identical spinning solutions were used for both the core and shell phases. During electrospinning, the shell layer, which is directly exposed to the external environment, experiences greater drag forces and undergoes rapid solidification. This facilitates a higher degree of polymer chain orientation in the shell region than in the core. As a result, despite having the same chemical composition, the resulting nanofibers exhibited distinct core-shell characteristics owing to differences in molecular orientation, as depicted in Fig. 1(a). $CsCuCl_3$ nanoparticles, a class of copper-based halide perovskites, have been reported to effectively promote the formation of the electroactive β-phase when incorporated into a piezoelectric PVDF matrix.[37] Accordingly, we synthesized $CsCuCl_3$ nanoparticles *via* a facile solvothermal route and integrated them into the PVDF spinning solution to fabricate core-shell structured PVDF/$CsCuCl_3$ piezoelectric nanofiber membranes. The morphology of the synthesized $CsCuCl_3$ nanoparticles observed *via* SEM revealed a well-defined hexagonal shape (Fig. S1 in the electronic supplementary information, ESI). In addition, XRD analysis was performed to confirm the phase purity of the nanoparticles. The diffraction peaks matched well with the standard pattern reported in the literature, verifying the phase-pure nature of the $CsCuCl_3$ nanoparticles (Fig. S2 in ESI).[38] Fig. 1(b) shows a digital photograph of the as-prepared PVDF/$CsCuCl_3$ core-shell nanofiber membrane (2 wt% $CsCuCl_3$), fabricated using a coaxial stainless-steel needle with 23-gauge (ID: 0.35 mm) inner and 18-gauge (ID: 0.9 mm) outer needles. For convenience, this sample is referred to as the PCs-23/18 fibrous membrane. Notably, the membrane demonstrated excellent flexibility, as evidenced by its ability to be folded into the shape of a butterfly. The surface morphology and cross-sectional structure of the membrane are shown in the SEM images in Figs. 1(c) and 1(d), respectively. The nanofibers exhibited uniform morphology with an average diameter of approximately 700 nm, and the overall thickness of the membrane was approximately 600 μm.

To systematically investigate the influence of both compositional modification and spinneret configuration on the piezoelectric performance of the nanofiber films, three additional samples were fabricated: PVDF-23 (pure PVDF nanofibers prepared using a single-needle spinneret with a gauge of 23), PCs-23 (PVDF/$CsCuCl_3$ nanofibers *via* single-needle spinneret with a gauge of 23), and PCs-25/18 (PVDF/$CsCuCl_3$ nanofibers *via* coaxial spinneret with inner/outer gauges of 25 and 18, respectively), as shown in Fig. S3 (in ESI). All PVDF/$CsCuCl_3$ composite fibrous membranes (PCs-23, PCs-23/18, and PCs-25/18) were prepared with a $CsCuCl_3$ content of 2 wt%. Detailed specifications of the spinnerets employed for each sample are summarized in Table S1 (in ESI).

Fig. 2(a) shows the FTIR spectra of the as-prepared fibrous membranes. The characteristic absorption peaks of the nonpolar α-phase (763 cm^{-1}) and the electroactive β-phase (840, 1275, 1402, and 1433 cm^{-1}) are identified[39,40]. The relative fraction of the β-phase can be quantitatively calculated from the intensity ratio of these characteristic peaks. These spectra were used to quantitatively calculate the relative β-phase contents of the fibrous membranes. The XRD patterns (Fig. 2b) reveal a pronounced enhancement of the β-phase diffraction peak at 20.6° in the PCs-23/18 sample compared to both pristine PVDF (PVDF-23) and the single-needle composite (PCs-23). This enhancement is attributed to a confined crystallization effect induced by the core-shell fiber architecture, where strong interfacial interactions between $CsCuCl_3$ nanoparticles and the PVDF matrix promote molecular chain alignment and β-phase formation.[37] DSC curves of various fibrous membranes are presented in Fig. 2(c). The melting temperature (T_m) of PVDF-23 was 162.93 °C. Upon incorporation of $CsCuCl_3$ nanoparticles, T_m increases due to the nucleating effect of the nanoparticles, which facilitates PVDF crystallization. Specifically, the T_m values for PCs-23, PCs-23/18, and PCs-25/18 are 163.99, 164.41, and 164.20 °C, respectively. Furthermore, a slight increase in crystallinity was observed in the

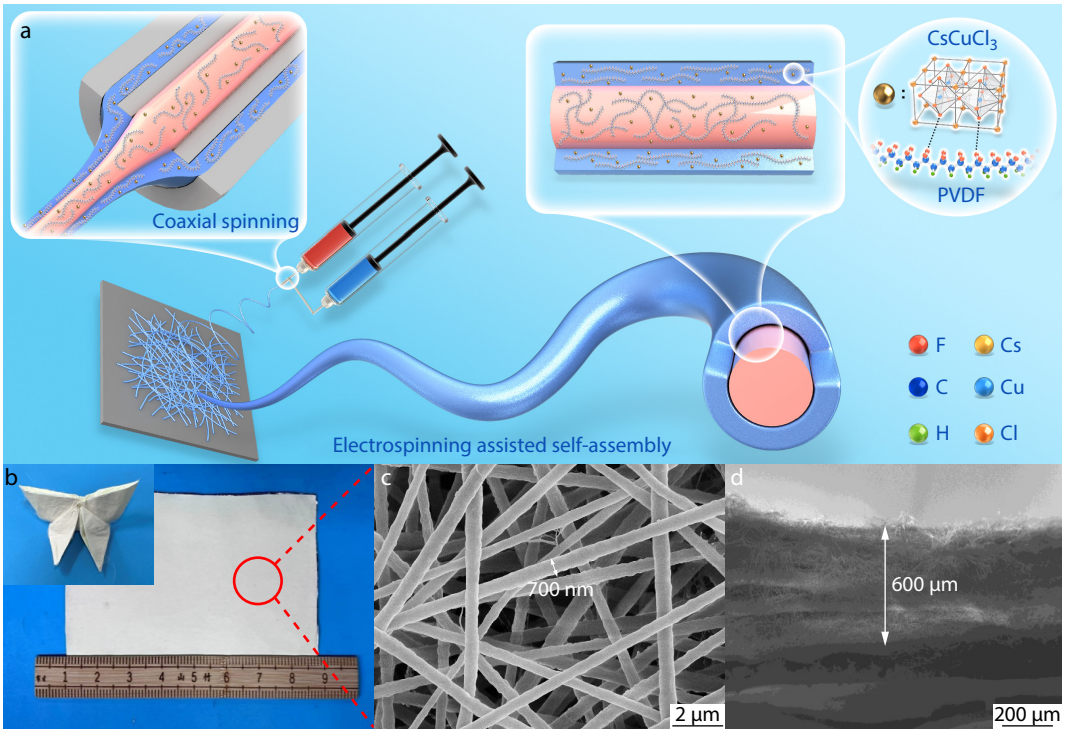

Fig. 1 (a) Schematic illustration of the coaxial electrospinning process and the resulting core-shell structure of the PVDF/$CsCuCl_3$ nanofibers; (b) Digital photograph of PVDF/$CsCuCl_3$ core-shell nanofiber film, including a demonstration of its flexibility by folding into a butterfly shape; (c, d) SEM images showing the microscopic surface morphology and cross-sectional morphology of nanofiber film.

coaxially electrospun samples (PCs-23/18 and PCs-25/18) compared with that of PCs-23. This enhancement is attributed to the higher degree of polymer chain orientation achieved through the coaxial spinning process, which promotes more ordered crystalline structures within the nanofibers[41].

Both the relative content of the β-phase and the degree of crystallinity are critical factors that influence the piezoelectric performance of the fabricated fibrous membranes. According to previous studies,[42] the relative fraction of the β-phase in each nanofiber sample can be calculated using the following equation:

$$F(\beta) = \frac{A_\beta}{A_\beta + (K_\beta/K_\alpha)A_\alpha} \quad (1)$$

where A_β and A_α are the absorbances at 840 and 763 cm^{-1} (Fig. 2a), corresponding to the β- and α-phases, respectively. K_α and K_β represent the absorption coefficients at 763 cm^{-1} (6.1×10^4 cm^2/mol) and 840 cm^{-1} (7.7×10^4 cm^2/mol), respectively. Additionally, the crystallinity (χ) of the nanofiber membranes can be determined by

$$\chi(\%) = \frac{\Delta H_m}{\Delta H_m^0} \times 100\% \quad (2)$$

where ΔH_m is the change of melting enthalpy of the sample, and ΔH_m^0 represents the fusion heat of pure PVDF, which has been determined to be 104.7 J/g, corresponding to the 100% crystalline PVDF. ΔH_m was calculated using the following equation:

$$\Delta H_m = \frac{S}{W} \quad (3)$$

where S is the integral area of the melting enthalpy in the DSC curve and W is the sample weight.

Fig. 2(d) presents the calculated β-phase contents and crystallinities of the various fibrous membranes. The β-phase fractions of PCs-23 (89.8%), PCs-23/18 (87.7%), and PCs-25/18 (85.8%) were significantly higher than those of pristine PVDF-23 (83.4%), confirming that the incorporation of $CsCuCl_3$ nanoparticles effectively promoted phase transformation from the non-piezoelectric α-phase to the electroactive β-phase. Similarly, the crystallinity of the composite nanofiber films increased upon CsCuCl incorporation. The calculated crystallinities of PCs-23 (50.5%), PCs-23/18 (52.3%), and PCs-25/18 (51.2%) were higher than that of PVDF-23 (49.3%). This enhancement can be attributed to the nucleating effect of $CsCuCl_3$ nanoparticles, which facilitates PVDF chain alignment and crystallization, thereby improving the overall degree of crystallinity.

It is evident that the $CsCuCl_3$ content also influences the formation of the piezoelectric active β-phase. In Fig. S4 (in ESI), we present the calculated β-phase content as a function of the $CsCuCl_3$ content for different PCs-23 nanofiber membranes. The β-phase content initially increases with the addition of $CsCuCl_3$ and reaches a maximum at 2 wt%. This enhancement can be attributed to the nucleating effect of well-dispersed $CsCuCl_3$ nanoparticles. However, at higher loadings, particle aggregation may occur, which disrupts the molecular alignment of the PVDF chains and consequently hinders the β-phase formation. Based on these findings, the $CsCuCl_3$ content was fixed at 2 wt% for the other samples.

The mechanical properties of the prepared fibrous films are compared in Fig. S5 (in ESI). Clearly, the addition of $CsCuCl_3$

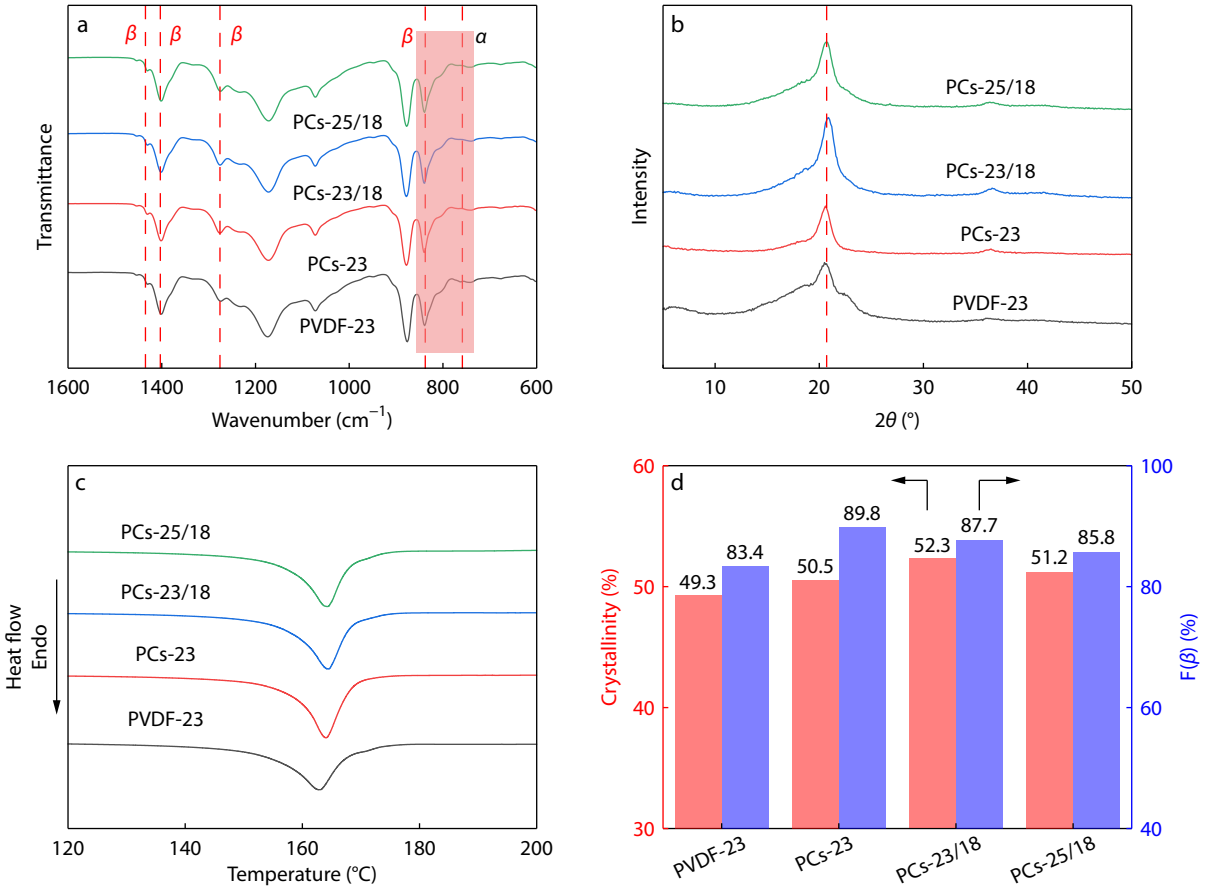

Fig. 2 Characterizations of the $CsCuCl_3$/PVDF nanofibrous membrane. (a) FTIR spectra (transmittance mode) of different fiber membranes in the range of 650–1500 cm^{-1}; (b) XRD patterns of the different fiber membranes; (c) DSC curves of different fiber membranes; (d) Calculated crystallinity and β-phase content of different fiber membranes.

could enhances the mechanical performance of the fibrous films. Specifically, the tensile strength increases from 2.0 MPa in PVDF-23 to 3.7 MPa in PCs-23/18, while the elongation at break improved from 98% to 164%. This mechanical reinforcement is likely due to strong hydrogen bonding interactions between the PVDF chains and $CsCuCl_3$ nanoparticles,[37] which contribute to better stress transfer within the composite matrix. In addition, the surface wettability of the fibrous membranes was evaluated using water contact angle measurements, as shown in Fig. S6 (in ESI). All the samples exhibited good hydrophobicity, with contact angles ranging from 128.6° to 135.2°, indicating that the surface characteristics of the membranes are suitable for applications requiring moisture resistance.

Piezoelectric Performance of PENGs Assembled From Different Nanofiber Membranes

PENGs were fabricated by placing two copper electrodes on opposite sides of the nanofibrous membranes, enabling their use in energy-harvesting and pressure-sensing applications. A linear motor was employed to apply a constant compressive force to the devices and the resulting open-circuit voltage (V_{oc}) and short-circuit current (I_{sc}) were recorded using a digital electrostatic meter. Figs. 3(a) and 3(b) show the measured V_{oc} and I_{sc} values for different PENGs under a constant pressure of 10 N. A dramatical enhancement in output performance is observed after incorporating 2 wt% $CsCuCl_3$ nanoparticles into the PVDF matrix. Specifically, the V_{oc} of the PCs-23-based PENG reaches 48 V, representing an increase of approximately 220% compared to the PVDF-23-based PENG. The influence of $CsCuCl_3$ content on the piezoelectric performance of PCs-23-based PENGs is shown in Fig. S7 (in ESI). Consistent with the trend in β-phase content, Fig. S4 (in ESI), the highest voltage output was achieved at a $CsCuCl_3$ loading of 2 wt%, confirming its optimal concentration for enhancing piezoelectric activity. Interestingly, PENGs based on coaxially electrospun nanofibers, namely PCs-23/18 and PCs-25/18, exhibit even higher output performance than their single-needle counterparts (PCs-23). Notably, the V_{oc} of the PCs-23/18-based PENG was 75 V, which was about 27 V (approximately 56%) higher than that of the PCs-23-based PENG. Considering that both PCs-23 and PCs-23/18 have identical compositions, this enhancement can only be attributed to the core-shell fiber structure formed through coaxial electrospinning. The improved performance arises from the higher degree of polymer chain orientation induced by the coaxial spinneret, which facilitates the increased crystallinity and higher fraction of the electroactive β-phase (Fig. 2d). These findings suggest that the piezoelectric output can be significantly enhanced by tailoring the fiber structure, specifically by adopting coaxial electrospinning, without altering the material composition. Additional comparisons were performed to verify the universality of this

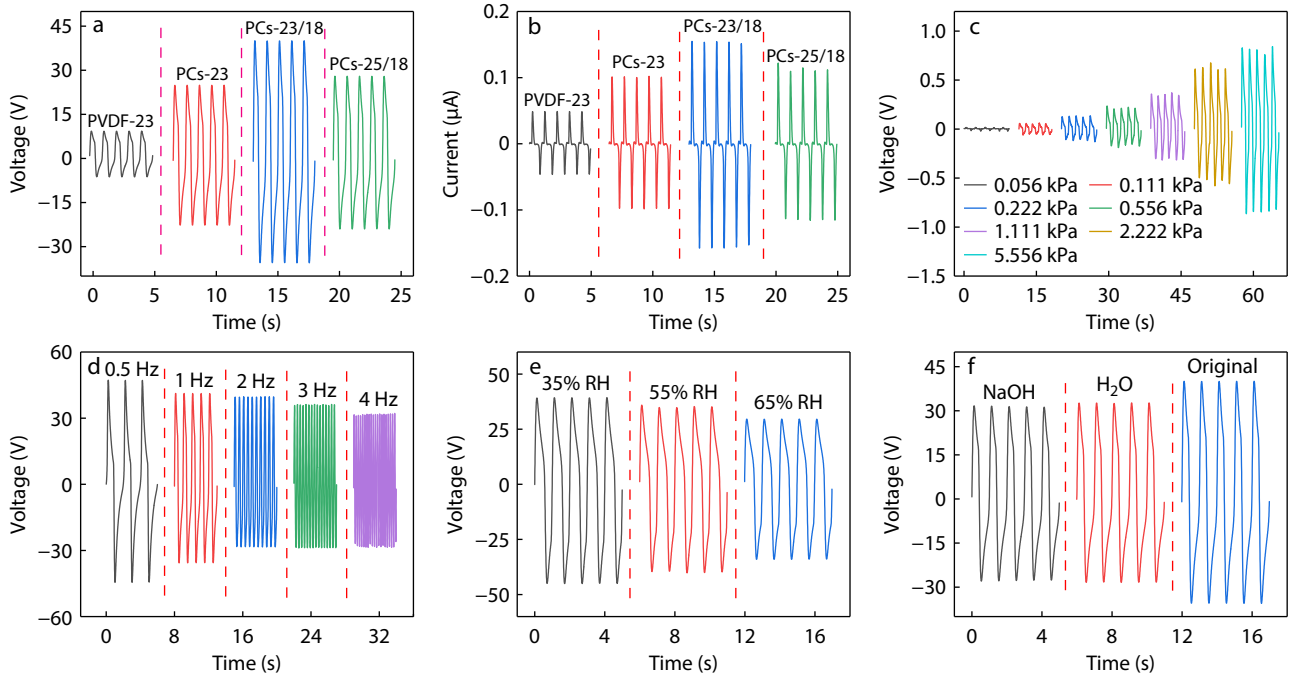

Fig. 3 (a) The open-circuit voltage and (b) short-circuit current of different PENGs; (c) Voltage output of PCs-23/18 based PENG under varying pressure forces; (d) Voltage output of the PCs-23/18-based PENG at different frequencies; (e) Voltage output of the PCs-23/18-based PENG under different ambient humidity levels; (f) Comparison of the voltage output of the PCs-23/18-based PENG before and after soaking in water or NaOH solution.

structural effect. As shown in Fig. S8 (in ESI), replacing the single-needle spinneret (23-gauge) with a coaxial spinneret (23-gauge inner/18-gauge outer) for pure PVDF electrospinning can result in an increase in V_{oc} from 16 V to 24 V (about 50% improvement). Similarly, PVDF/ZnO composite fibers with a ZnO content of 4 wt% were prepared using both single-needle (PZn-23) and coaxial (PZn-23/18) spinnerets. The PZn-23/18-based PENG produced a V_{oc} of 81 V, which was significantly higher than that of the 64 V generated by the PZn-23-based PENG (Fig. S9 in ESI). These results further confirm the universal nature of the coaxial electrospinning strategy for enhancing the piezoelectric performance of polymer-based PENGs, regardless of the specific filler used.

Because the PCs-23/18-based PENG exhibited optimal piezoelectric performance, it was selected for further examination. Figs. 3(c) and 3(d) show the output voltages of the PCs-23/18-based PENG under varying pressure forces and frequencies, respectively. As the applied force increased, the output voltage also increased (Fig. 3c). However, a slight decrease in the voltage output was observed as the frequency further increased from 0.5 Hz to 4.0 Hz (Fig. 3d). This decline is attributed to charge accumulation at higher frequencies, which reduces the effective output voltage.[43,44] Previous studies have reported that ambient humidity can significantly affect electron transport in PENGs, leading to a substantial reduction in piezoelectric output.[45] Fig. 3(e) shows the piezoelectric output of the PCs-23/18-based PENG under varying ambient humidity levels while maintaining a constant pressure (10 N) and frequency (1 Hz). Only a slight decrease in the output was observed as the humidity increased from 35% to 65%, indicating that the PENG possesses good moisture resistance and can operate reliably even in high-humidity environments. This moisture resistance was likely due to the strong hydrophobicity of the fibrous film, which effectively prevented water penetration. Furthermore, the PENG was soaked in either water or 30% NaOH solution for 6 h, and its piezoelectric performance was subsequently tested (Fig. 3f). Although the output voltage slightly decreased compared to that of the original device, it still produced a stable and high voltage under pressure, demonstrating good chemical and environmental durability.

To further evaluate the energy-harvesting potential of the PENG, its output voltage and current were measured under various external load resistances. As shown in Figs. 4(a) and 4(b), the output voltage increases steadily, whereas the output current decreases correspondingly as the load resistance increases. Accordingly, the calculated power density exhibits a distinct peak, as expected (Fig. 4c). Specifically, for our optimized composite film, the maximum power density ($P = U^2/R$) reached 0.96 μW/cm^2 at a matched load resistance of 300 MΩ. When the PENG is connected to a capacitor, it can continuously charge, as illustrated in Figs. 4(d) and 4(e). After 80 seconds of charging, the voltages of the capacitors reached 1.60 V (2.2 μF), 1.35 V (3.3 μF), and 1.02 V (4.7 μF), respectively. To assess the long-term durability of the device, the PENG underwent 5000 cycles of compression and release at 2 Hz and 10 N (Fig. 4f). Remarkably, and the output voltage remained stable throughout the entire cycling process, indicating excellent mechanical and electrical stability.

Applications of PCs-23/18 Based PENG

The application of PENG in computer game

By capitalizing on PENG's energy-harvesting capability of the

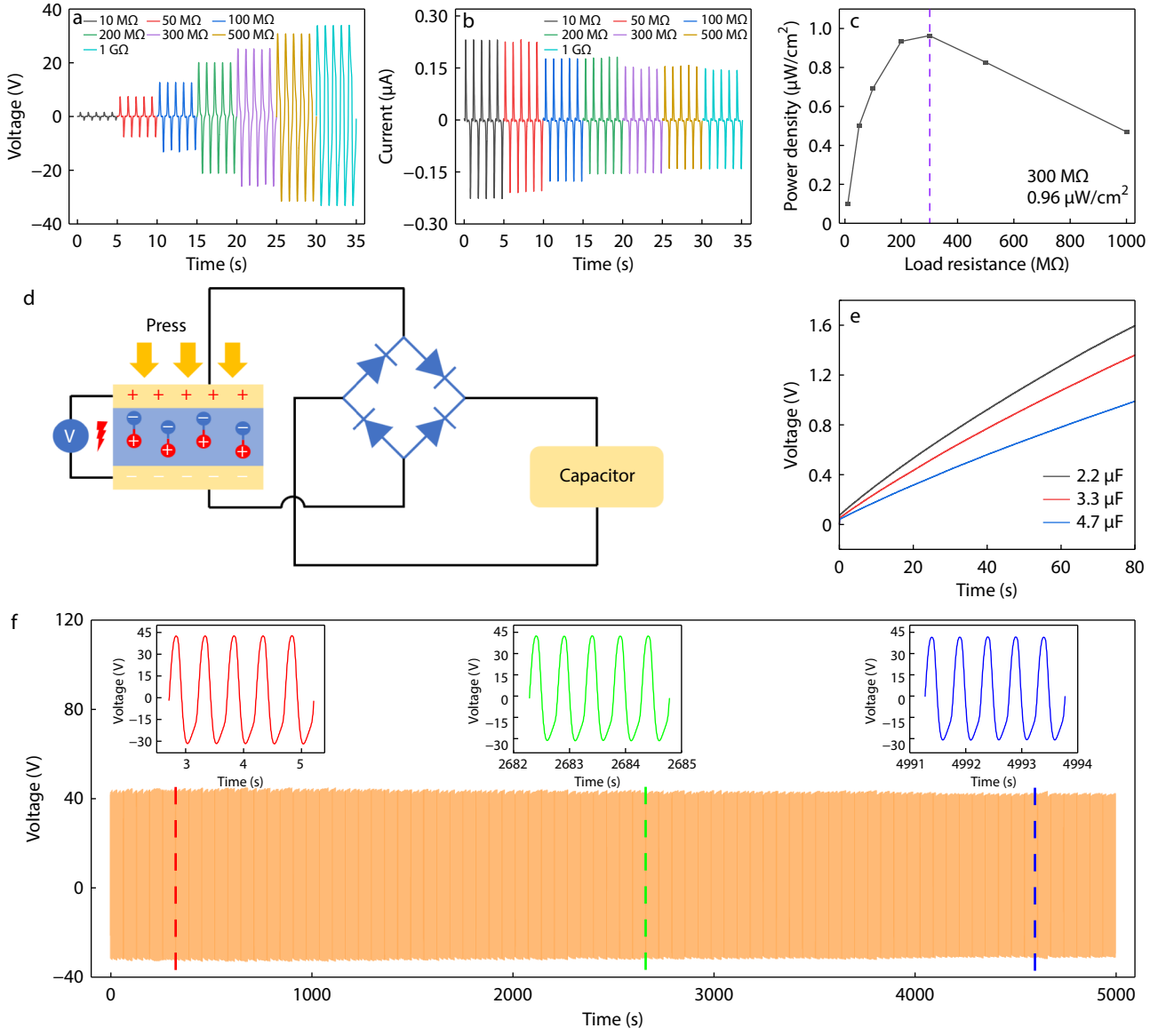

Fig. 4 (a, b) Output voltage and current of the PCs-23/18 based PENG under varying external load resistances; (c) Power density of the PENG as a function of load resistance; (d) Equivalent circuit diagram of the capacitor charging system driven by the PENG; (e) Charging curves of different capacitors (2.2, 3.3, and 4.7 μF) powered by the PENG; (f) Long-term operational stability of the PENG after 5000 compression-release cycles at 2 Hz and 10 N.

PENG, we developed an intelligent keyboard matrix (Fig. 5a). The system integrates mechanical sensors with arrayed PENG elements that transduce key presses into electrical signals, processed by a custom analog front-end circuit (Fig. 5b) featuring a 3.3 V power supply with current-limiting resistors, reverse-biased LEDs for optical feedback, and parallel PENG connections enabling voltage-divider functionality. Digital processing is managed by a microcontroller unit (MCU) equipped with a 12-bit ADC for high-resolution signal quantization, while human-machine interaction is facilitated through a serial communication protocol that transmits keystroke data to host computers. Functional validation demonstrated precise four-directional control in a gaming application (Fig. 5c), where PENG-equipped keys governed the snake movement commands. This implementation shows the self-powered sensor's potential for human-machine interaction.

The application of PENG in speech signal recognition

The exceptional performance characteristics of PENG devices were synergistically combined with deep learning algorithms to establish their efficacy in human-machine interaction applications. Initial evaluations demonstrated remarkable mechanical sensitivity, with the PENG sensor detecting minute pressure variations, as low as 0.056 kPa. This sensitivity is particularly advantageous for physiological monitoring in which subtle biomechanical signals must be resolved. Human speech production involves complex vibro-acoustic dynamics. Vocal-fold oscillations during phonation generate vibrational waves that propagate through the vocal tract, undergoing resonant modulation in the pharynx and oral cavity. Concurrently, the extralaryngeal tissues, particularly in the laryngeal prominence region,

https://doi.org/10.1007/s10118-026-3587-8

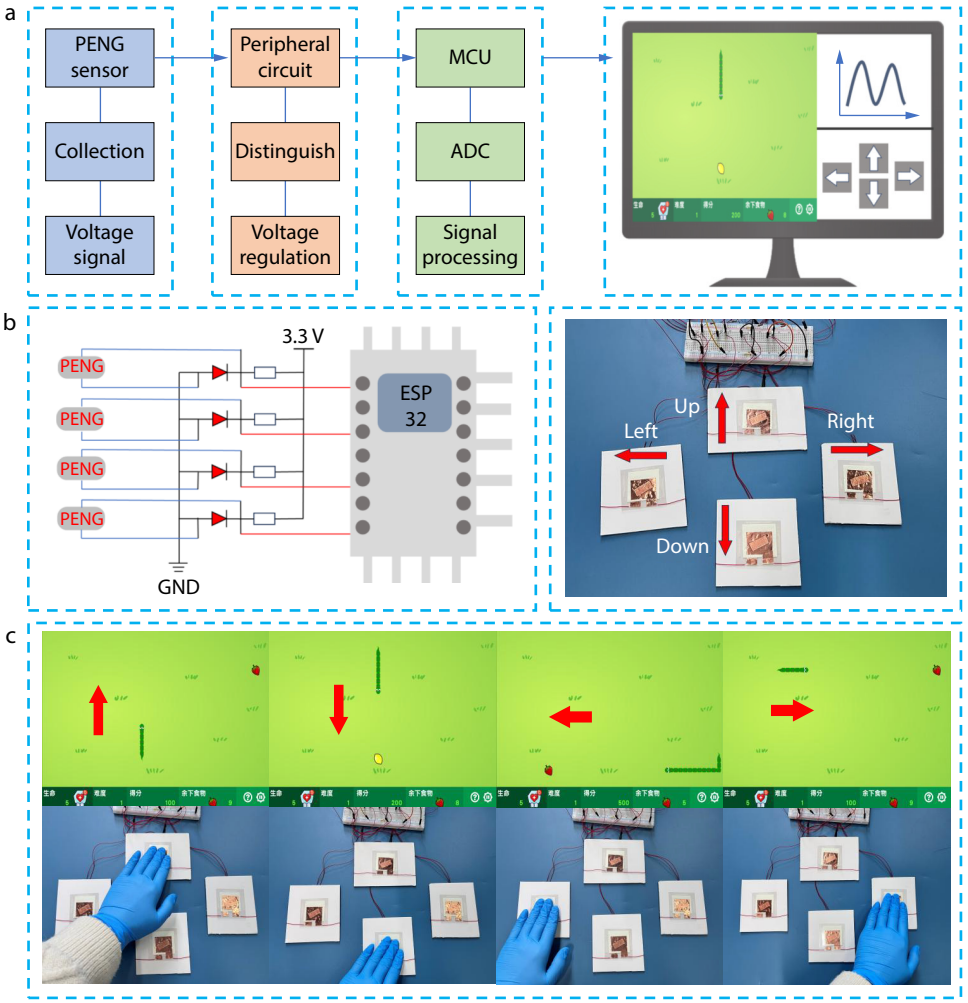

Fig. 5 The application of PENG in computer game. (a) The overall flowchart of PENG devices applied to game; (b) Circuit diagram of device connection and schematic diagram of intelligent array keyboard; (c) Schematic diagram of intelligent array keyboard controlling the four directions of snake movement.

exhibit synchronized surface vibrations that correlate with vocalization patterns. To capture these biomechanical speech signatures, we implemented a throat-mounted PENG sensor configuration (Fig. 6a). The system was trained to recognize eight distinct commands: "Open," "Close," "Up," "Down," "Next," "Previous," "Left" and "Right." The deep learning framework comprises a 1D convolutional neural network (1D-CNN) optimized for temporal feature extraction (Fig. 6b).

The network uses raw waveform inputs of length 5000, which are first reshaped into a (5000, 1) format to be compatible with the convolutional layers. The model architecture comprised three consecutive convolutional blocks. Each block included a 1D convolutional layer with 64, 128, and 256 filters, respectively, using a kernel size of 3 and ReLU activation functions, followed by a max-pooling layer with a pooling size of 2 to progressively reduce the temporal resolution and extract hierarchical features. L2 regularization was applied to all the convolutional layers to prevent overfitting. After convolutional feature extraction, the output is flattened and passed through a fully connected dense layer with 512 neurons, regularized, and followed by a dropout layer (dropout rate=0.5) to further enhance generalization. Finally, the network concludes with a softmax output layer containing eight neurons corresponding to eight speech categories.

A dedicated dataset containing 20 recordings per command (total N=160) was constructed for training. Each command produced unique voltage waveform morphologies, particularly in terms of the peak amplitude and temporal distribution characteristics (Fig. 6c). Temporal alignment across samples was achieved through the zero-padding of shorter recordings to match the longest duration. During training, as shown in Figs. 6(d) and 6(e), the model exhibited a stable convergence behavior, with the loss function decreasing progressively and the classification accuracy steadily increasing over the epochs. This indicates that the network effectively learns discriminative features from raw speech signals. After convergence, the performance of the model was evaluated using a confusion matrix for the test dataset (Fig. 6f). The confusion matrix showed that most samples were correctly classified, with minimal misclassification between the different speech categories. The overall classification accuracy exceeded 99%, demonstrating the effectiveness and reliability of the proposed 1D-CNN-based approach in recognizing speech signals acquired from a flexible capacitive sensor.

https://doi.org/10.1007/s10118-026-3587-8

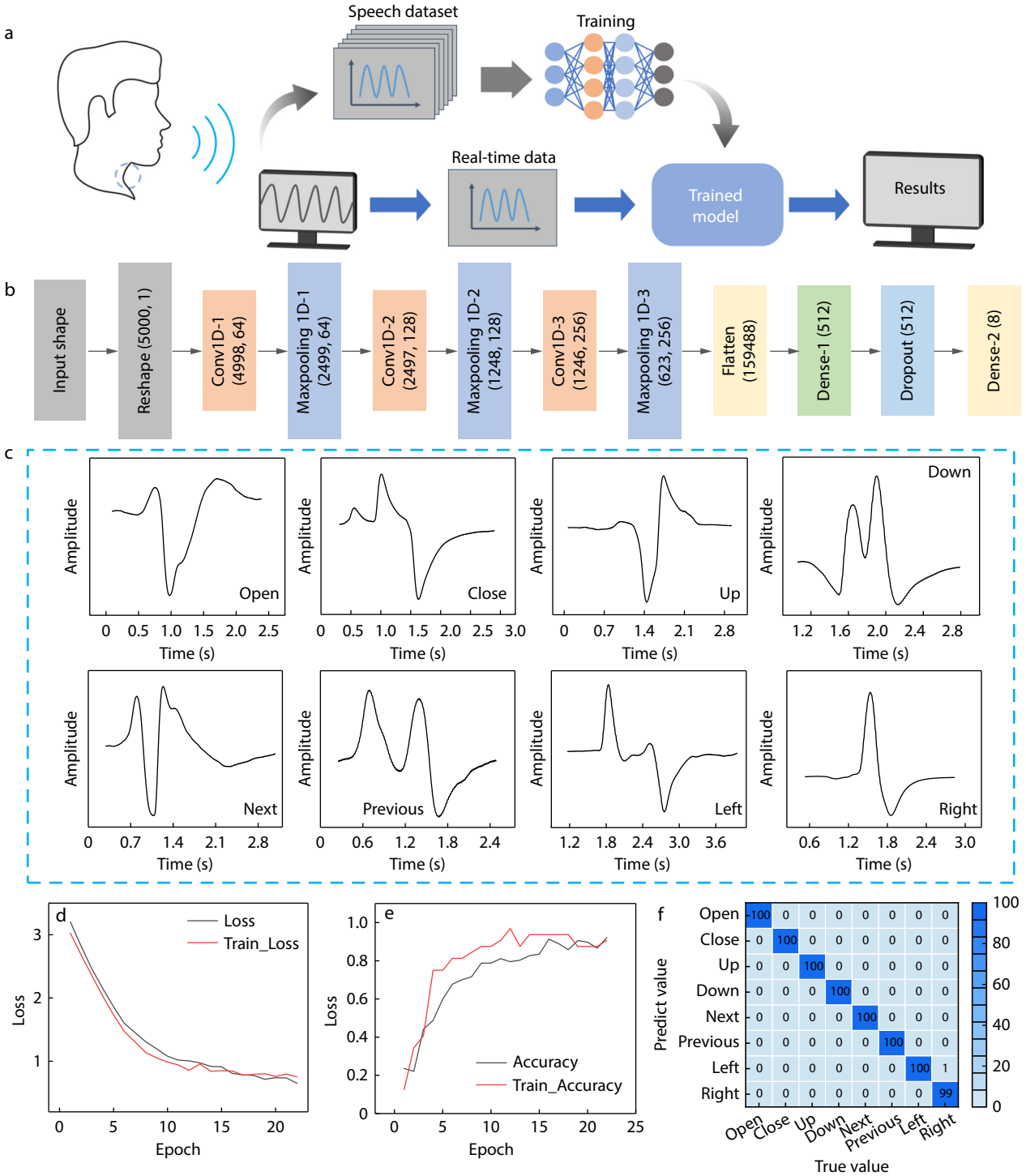

Fig. 6 The application of PENG in speech signal recognition. (a) Brief speech recognition flowchart; (b) 1D-CNN algorithm program flow chart; (c) The voltage output signal obtained from eight words stuck on the throat. Network architecture diagram based on customized 1D-CNN algorithm. As the training time increases, the loss (d) gradually decreases, while the accuracy (e) gradually increases; (f) Confusion matrix diagram of speech recognition accuracy.

CONCLUSIONS

In summary, we report a significant finding that with the same composition, nanofiber films fabricated using a coaxial spinneret to create a core-shell structure exhibit substantially higher piezoelectric output than traditional nanofiber films produced *via* single-needle electrospinning. This enhancement is observed not only in pure PVDF nanofiber films but also in PVDF-based hybrid nanofiber systems such as PVDF/$CsCuCl_3$ and PVDF/ZnO. The improved performance can be attributed to the

coaxial electrospinning process, which induces greater polymer chain alignment in the shell layer, leading to increased crystallinity and a higher proportion of the piezoelectric-active β-phase. As a result, the PENG based on the core-shell structured PVDF/$CsCuCl_3$ nanofiber film (2 wt%) achieves a high output voltage of 75 V, which is approximately a 60% increase compared to the conventional PVDF/$CsCuCl_3$ nanofiber-based PENG. Owing to its excellent piezoelectric performance, the device demonstrates great potential for application in human-machine interaction systems. This study presents a novel and effective strategy for significantly enhancing the piezoelectric performance of polymer-based PENGs, offering promising prospects for their integration into self-powered electronic devices.

Conflict of Interests

The authors declare no interest conflict.

Electronic Supplementary Information

Electronic supplementary information (ESI) is available free of charge in the online version of this article at http://doi.org/10.1007/s10118-026-3587-8.

Data Availability Statement

Data supporting the findings of this study are available from the corresponding author upon reasonable request.

ACKNOWLEDGMENTS

This work was financially supported by the Key Project of Jiangsu Provincial Key Laboratory of Biomass Energy and Materials (No. JSBEM-S-202303), the National Natural Science Foundation of China (No. 52273070), and the Natural Science Fund of Zhejiang Province (No. LRG25E030003).

REFERENCES

1 Abdolmaleki, H.; Haugen, A. B.; Buhl, K. B.; Daasbjerg, K.; Agarwala, S. Interfacial engineering of pvdf-trfe toward higher piezoelectric, ferroelectric, and dielectric performance for sensing and energy harvesting applications. *Adv. Sci.* **2023**, *10*, 2205942.
2 Han, Y. Q.; Lei, Z. Y.; Wu, P. Y. Mxene nanosheet-enhanced ionotronic hydrogels for wireless powering and noncontact sensing. *Chinese J. Polym. Sci.* **2025**, *43*, 572−580.
3 Yi, Z.; Liu, Z.; Li, W.; Ruan, T.; Chen, X.; Liu, J.; Yang, B.; Zhang, W. Piezoelectric dynamics of arterial pulse for wearable continuous blood pressure monitoring. *Adv. Mater.* **2022**, *34*, 2110291.
4 Zhao, C. X.; Guo, M.; Mao, J.; Li, Y. T.; Wu, Y. P.; Guo, H.; Xiang, D.; Li, H. Self-healing, stretchable, temperature-sensitive and strain-sensitive hydrogel-based flexible sensors. *Chinese J. Polym. Sci.* **2022**, *41*, 334−344.
5 Song, X.; Yi, B.; Chen, Q.; Zhou, Y.; Cho, H.; Hong, Y.; Chung, S.; You, L.; Li, S.; Hong, J. Machine learning-powered ultrahigh controllable and wearable magnetoelectric piezotronic touching device. *ACS Nano* **2024**, *18*, 16648−16657.
6 Hu, C. N.; He, J.; He, Y. T.; Peng, Y. J. Anti-freezing conductive gelatin hydrogel reinforced with polypyrrole-decorated cellulose nanofibers for strain sensors and triboelectric nanogenerators. *Chinese J. Polym. Sci.* **2025**, *43*, 2083−2093.
7 Zarzoso, M.; Mikhalchan, A.; Mocerino, D.; Romero-Rodriguez, P.; Losada, R.; Vilatela, J. J.; González, C. Strain sensing of structural composites by integrated piezoresistive cnt yarn sensors. *Compos. Part B* **2024**, *286*, 111752.
8 Xiong, Z.; Huang, J.; Chen, J.; Liu, Z.; Zhu, Y.; Sui, G.; Liu, Z. Synergy of hierarchical structures and multiple conduction mechanisms for designing ultra-wide linear range pressure sensors. *Chem. Eng. J.* **2025**, *503*, 158359.
9 Tu, S.; Xi, Y.; Cui, X.; Xu, Z.; Liu, Z.; Zhu, Y. Skin-inspired interlocked microstructures with soft-hard synergistic effect for high-sensitivity and wide-linear-range pressure sensing. *Chem. Eng. J.* **2024**, *496*, 154083.
10 Wang, X. Y.; Bai, J. J.; Yang, T. J.; Yu, X. D. Organic-inorganic hydrogel strain sensors based on methacryloyl ethoxy trimethyl ammonium chloride and bentonite. *Chinese J. Polym. Sci.* **2025**, *43*, 1904−1916.
11 Wang, J.; Chen, Y.; Tu, S.; Cui, X.; Chen, J.; Zhu, Y. Recent advances in flexible iontronic pressure sensors: materials, microstructure designs, applications, and opportunities. *J. Mater. Chem.* **2024**, *12*, 14202−14221.
12 Li, J.; Guo, K.; Li, P.; Liu, Z.; Lin, H.; Feng, Z.; Wang, X.; Ran, F.; Xue, K.; Wu, Y.; Wei, K.; Yang, J. High-sensitivity capacitive pressure sensor based on novel and bio-inspired hybrid dielectric layer for medical exercise rehabilitation. *Compos. Part B.* **2025**, *303*, 112565.
13 Wang, Y.; Hou, S.; Li, T.; Jin, S.; Shao, Y.; Yang, H.; Wu, D.; Dai, S.; Lu, Y.; Chen, S.; Huang, J. Flexible capacitive humidity sensors based on ionic conductive wood-derived cellulose nanopapers. *ACS Appl. Mater. Interfaces* **2020**, *12*, 41896−41904.
14 He, P.; Zhong, Y.; Zhang, B.; Ma, L.; Fang, J.; Li, J. Composite porous polyimide film-based piezoelectric sensors for harsh environments. *ACS Appl. Polym. Mater.* **2025**, *7*, 10541−10551.
15 Wu, Z.; Huang, J.; Zhao, Y.; Ding, X.; Chen, J.; Liu, Z.; Liu, Z.; Zhu, Y. Lotus leaf-inspired superhydrophobic piezoelectric nanofiber films for moisture-proof pressure sensing and energy harvesting. *Chem. Eng. J.* **2025**, *504*, 158874.
16 Ham, S. S.; Lee, G. J.; Hyeon, D. Y.; Kim, Y. G.; Lim, Y. W.; Lee, M. K.; Park, J. J.; Hwang, G. T.; Yi, S.; Jeong, C. K.; Park, K. I. Kinetic motion sensors based on flexible and lead-free hybrid piezoelectric composite energy harvesters with nanowires-embedded electrodes for detecting articular movements. *Compos. Part B.* **2021**, *212*, 108705.
17 Li, H. P.; Liang, J. M.; Song, H. Y.; Zhu, H. Q.; Zhao, W. P.; Wang, S. J.; Zhang, H.; Yan, S. K. Poly(vinylidene fluoride) of different β-phase/γ-phase ratio prepared by heat controlled spin coating and potassium bromide as nucleating agent. *Chinese J. Polym. Sci.* **2025**, *43*, 769−777.
18 Huang, Y. Z.; Liu, Z.; Li, L. W.; He, H. Z.; Wang, Z. L.; Qu, J. P.; Chen, X.; Huang, Z. X. Giant piezoelectric coefficient of polyvinylidene fluoride with rationally engineered ultrafine domains achieved by rapid freezing processing. *Adv. Mater.* **2024**, *37*, 2412344.
19 Wu, L.; Huang, J.; Chen, Y.; Wang, T.; Chen, J.; Chang, X.; Liu, Z.; Liu, Z.; Zhu, Y. Breathable and highly sensitive self-powered pressure sensors for wearable electronics and human-machine interaction. *Compos. Sci. Technol.* **2025**, *262*, 111078.
20 Lee, J. E.; Shin, Y. E.; Lee, G. H.; Kim, J.; Ko, H.; Chae, H. G. Polyvinylidene fluoride (PVDF)/cellulose nanocrystal (CNC) nanocomposite fiber and triboelectric textile sensors. *Compos. Part B.* **2021**, *223*, 109098.
21 Shaukat, R. A.; Cha, A.; Tamim, A. M.; Kim, H.; Hwang, G. T.; Lee, H. E.; Lin, Z. H.; Kim, K.; Jeong, C. K. Zeolite-decorated triboelectric sensors for heavy metal contaminant detection. *ACS Appl.*

Graphical Abstract

Hetero-structured Poly(vinylidene fluoride)/$CsCuCl_3$ Nanofiber Composite Film *via* Coaxial Electrospinning for Human-Machine Interaction

Yi-Kai Zhao, Yi Zou, Jie-Chun Zhou, Jin-Rong Huang, Jian-Wen Chen, Jin-Rui Huang, and Yu-Tian Zhu

Hangzhou Normal University; Institute of Chemical Industry of Forest Products, Chinese Academy of Forestry

Driven by improved polymer alignment and β-phase content, core-shell nanofibers produced *via* coaxial electrospinning exhibit substantially enhanced piezoelectric output, thereby offering a promising pathway to high-performance nanogenerators for human-machine interaction.

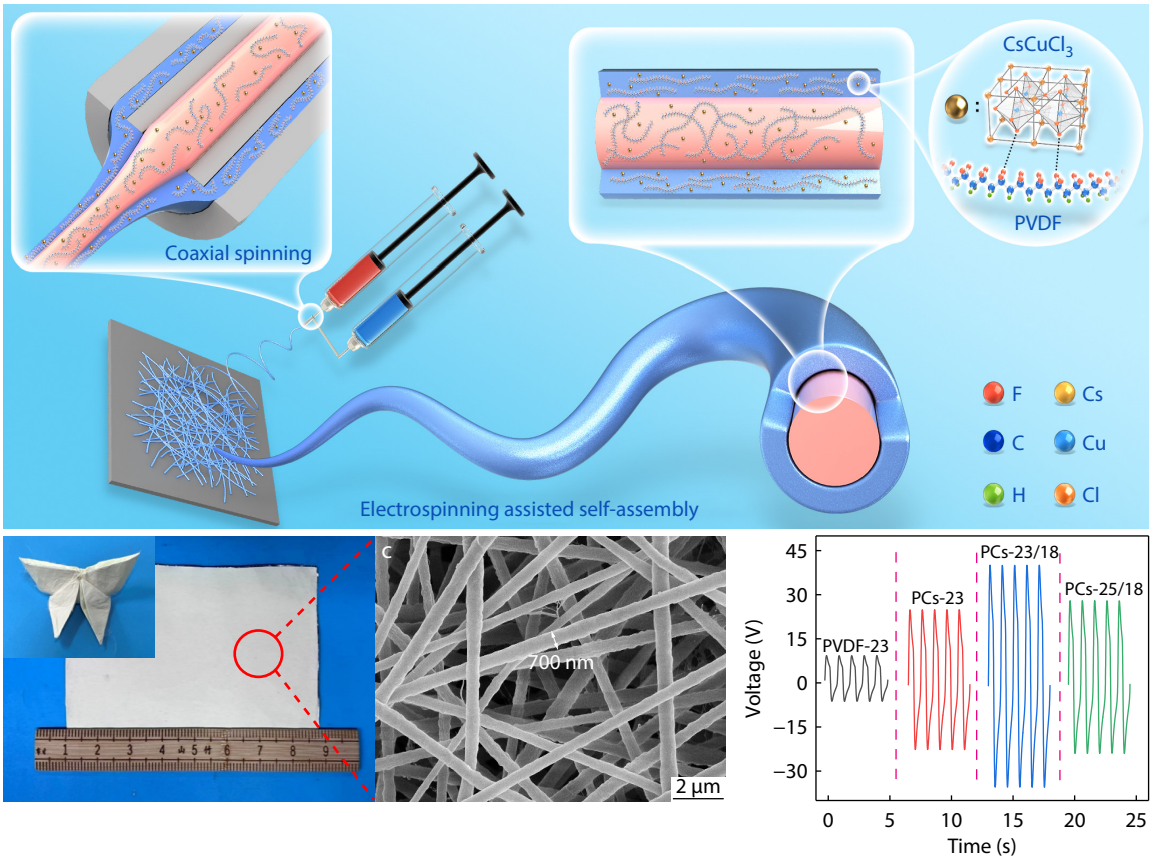

Chinese J. Polym. Sci., 2026 *https://doi.org/10.1007/s10118-026-3587-8*

Electron. Mater. **2025**, *7*, 3439–3447.

22 Yang, P.; Shi, Y.; Tao, X.; Liu, Z.; Dong, X.; Wang, Z. L.; Chen, X. Radical anion transfer during contact electrification and its compensation for charge loss in triboelectric nanogenerator. *Matter* **2023**, *6*, 1295–1311.

23 Maity, K.; Garain, S.; Henkel, K.; Schmeißer, D.; Mandal, D. Self-powered human-health monitoring through aligned PVDF nanofibers interfaced skin-interactive piezoelectric sensor. *ACS Appl. Polym. Mater.* **2020**, *2*, 862–878.

24 Du, B.; An, Y.; Huan, X.; Yang, L.; Zhao, Y. MWCNTs/C60 "Grape-like" nanostructures for enhancing piezoelectric performance in PVDF nanofibers through constructing localized conductive domains. *ACS Appl. Electron. Mater.* **2024**, *7*, 104–114.

25 Divya, S.; Ramasundaram, S.; Aruchamy, K.; Oh, T. H.; Levingstone, T.; Dunne, N. Piezoelectric nanogenerators from sustainable biowaste source: power harvesting and respiratory monitoring with electrospun crab shell powder-poly(vinylidene fluoride) composite nanofibers. *J. Colloid Interface Sci.* **2025**, *679*, 324–334.

26 Lei, C.; Hu, B.; Xu, R.; Cai, Q.; Shi, W. Influence of room-temperature-stretching technology on the crystalline morphology and microstructure of PVDF hard elastic film. *J. Colloid Interface Sci.* **2013**, *131*, 40077.

27 Wolfe, R. M. W.; Menon, A. K.; Fletcher, T. R.; Marder, S. R.; Reynolds, J. R.; Yee, S. K. Simultaneous enhancement in electrical

conductivity and thermopower of n-Type NiETT/PVDF composite films by annealing. *Adv. Funct. Mater.* **2018**, *28*, 1803275.
28 Song, S.; Zheng, Z.; Bi, Y.; Lv, X.; Sun, S. Improving the electroactive phase, thermal and dielectric properties of PVDF/graphene oxide composites by using methyl methacrylate-co-glycidyl methacrylate copolymers as compatibilizer. *J. Mater. Sci.* **2018**, *54*, 3832–3846.
29 Chang, C.; Tran, V. H.; Wang, J.; Fuh, Y. K.; Lin, L. Direct-write piezoelectric polymeric nanogenerator with high energy conversion efficiency. *Nano Lett.* **2010**, *10*, 726–31.
30 Yun, J. M.; Kwon, G.; Choi, J. H.; Kim, K. H. Advancing high-performance piezoelectric nanogenerators: simple electric field switching for orientated and aligned $BaTiO_3$/PDMS composite. *ACS Appl. Mater. Interfaces* **2024**, *16*, 14452.
31 Li, G. Y.; Li, J.; Li, Z. J.; Zhang, Y. P.; Zhang, X.; Wang, Z. J.; Han, W. P.; Sun, B.; Long, Y. Z.; Zhang, H. D. Hierarchical PVDF-HFP/ZnO composite nanofiber–based highly sensitive piezoelectric sensor for wireless workout monitoring. *Adv. Compos. Hybrid Mater.* **2021**, *5*, 766–775.
32 Cai, J.; Yan, L.; Seyedkanani, A.; Orsat, V.; Akbarzadeh, A. Nano-architected GaN metamaterials with notable topology-dependent enhancement of piezoelectric energy harvesting. *Nano Energy* **2024**, *129*, 109990.
33 Wu, J.; Qin, N.; Bao, D. Effective enhancement of piezocatalytic activity of $BaTiO_3$ nanowires under ultrasonic vibration. *Nano Energy* **2018**, *45*, 44–51.
34 Han, M.; Shen, W.; Corriou, J. P. Polydopamine-modified Mxene/cellulose nanofibers composite film for self-powered humidity sensing and humidity actuating. *Nano Energy* **2024**, *123*, 109445.
35 Fuh, Y. K.; Kuo, C. C.; Huang, Z. M.; Li, S. C.; Liu, E. R. A transparent and flexible graphene-piezoelectric fiber generator. *Small* **2016**, *12*, 1875–81.
36 Lan, B.; Zhong, C.; Wang, S.; Ao, Y.; Liu, Y.; Sun, Y.; Yang, T.; Tian, G.; Huang, L.; Zhang, J.; Deng, W.; Yang, W. A highly sensitive coaxial nanofiber mask for respiratory monitoring assisted with machine learning. *Adv. Fiber Mater.* **2024**, *6*, 1402–1412.
37 Zhi, C.; Zhang, S.; Wu, H.; Ming, Y.; Shi, S.; Io, W. F.; Meng, S.; Si, Y.; Fei, B.; Hao, J.; Hu, J. Perovskite nanocrystals induced core-shell inorganic-organic nanofibers for efficient energy harvesting and self-powered monitoring. *ACS Nano* **2024**, *18*, 9365–9377.
38 Mondal, S.; Poddar, S.; Bhattacharjee, S.; Maiti, S.; Banerjee, A.; Chattopadhyay, K. K. Lead free halide perovskite embedded PVDF based efficient mechanical energy harvester: self-driven respiratory sensor. *Nano Energy* **2023**, *115*, 108689.
39 Ponnamma, D.; Chamakh, M. M.; Alahzm, A. M.; Salim, N.; Hameed, N.; AlMaadeed, M. A. A. Core-shell nanofibers of polyvinylidene fluoride-based nanocomposites as piezoelectric nanogenerators. *Polymer* **2020**, *12*, 2344.
40 Mohana Rani, G.; Ranjith, K. S.; Ghoreishian, S. M.; Vilian, A. T. E.; Roh, C.; Umapathi, R.; Han, Y. K.; Huh, Y. S. Fabrication of MoS_2 petals-decorated PAN fibers-based triboelectric nanogenerator for energy harvesting and smart study room touch sensor applications. *Adv. Fiber Mater.* **2024**, *6*, 1825–1838.
41 Jiang, F.; Zhou, X.; Lv, J.; Chen, J.; Chen, J.; Kongcharoen, H.; Zhang, Y.; Lee, P. S. Stretchable, breathable, and stable lead-free perovskite/polymer nanofiber composite for hybrid triboelectric and piezoelectric energy harvesting. *Adv. Mater.* **2022**, *34*, 2200042.
42 Mondal, B.; Sarkar, R.; Saini, D.; Gupta, V.; Kundu, T. K.; Mandal, D. All-electrospun, water-resistant, breathable, wearable, and stable metal halide perovskite engineered electroactive polymer textiles for flexible piezoelectric nanogenerator. *Adv. Mater. Technol.* **2023**, *8*, 2300614.
43 Chen, H.; Zhou, L.; Fang, Z.; Wang, S.; Yang, T.; Zhu, L.; Hou, X.; Wang, H.; Wang, Z. L. Piezoelectric nanogenerator based on in situ growth all-inorganic $CsPbBr_3$ perovskite nanocrystals in PVDF fibers with long-term stability. *Adv. Funct. Mater.* **2021**, *31*, 2011073.
44 Jiao, H.; Lin, X.; Xiong, Y.; Han, J.; Liu, Y.; Yang, J.; Wu, S.; Jiang, T.; Wang, Z. L.; Sun, Q. Thermal insulating textile based triboelectric nanogenerator for outdoor wearable sensing and interaction. *Nano Energy* **2024**, *120*, 109134.
45 Pi, M.; Wu, D.; Wang, J.; Chen, K.; He, J.; Yang, J.; Zhang, D.; Chen, S.; Tang, X. Real-time and ultrasensitive humidity sensor based on lead-free Cs_2SnCl_6 perovskites. *Sens. Actuators B* **2022**, *354*, 131084.